frontiers | Frontiers in Materials

TYPE Original Research
PUBLISHED 09 May 2023
DOI 10.3389/fmats.2023.1180646

EDITED BY
Faryal Idrees,
University of the Punjab, Pakistan

REVIEWED BY
Jianhua Hou,
Yangzhou University, China
Abhigyan Dutta,
University of Burdwan, India

*CORRESPONDENCE
Muhammad Amin,
✉ muhammad.amin@phys.uol.edu.pk
Muhammad Tahir,
✉ tahir94@gmail.com

RECEIVED 06 March 2023
ACCEPTED 12 April 2023
PUBLISHED 09 May 2023

CITATION
Ali A, Amin M, Tahir M, Ali SS, Hussain A, Ahmad I, Mahmood A, Farooq MU and Farid MA (2023), g-C_3N_4/Fe_3O_4 composites synthesized via solid-state reaction and photocatalytic activity evaluation of methyl blue degradation under visible light irradiation.
Front. Mater. 10:1180646.
doi: 10.3389/fmats.2023.1180646

g-C_3N_4/Fe_3O_4 composites synthesized via solid-state reaction and photocatalytic activity evaluation of methyl blue degradation under visible light irradiation

Asghar Ali[1], Muhammad Amin[1]*, Muhammad Tahir[2,3]*, S. S. Ali[4], Asif Hussain[1,5], Imtiaz Ahmad[6], Asif Mahmood[7], M. Umer Farooq[8] and Muhammad Asim Farid[9]

[1]Department of Physics, The University of Lahore, Lahore, Pakistan, [2]Division of Science and Technology, University of Education Lahore, Vehari, Pakistan, [3]School of Chemical Engineering, University of Birmingham, Birmingham, United Kingdom, [4]School of Physical Sciences, University of the Punjab, Lahore, Pakistan, [5]College of Environmental Science and Engineering, Yangzhou University, Yangzhou, China, [6]Department of Physics and Astronomy, Texas Tech University, Lubbock, TX, United States, [7]Chemical Engineering Department, College of Engineering, King Saud University, Riyadh, Saudi Arabia, [8]Department of Chemistry, University of Education Lahore (Vehari Campus), Vehari, Pakistan, [9]Department of Physics, Division of Science and Technology, University of Education Lahore, Vehari, Pakistan

This study applied the solid-state reaction technique to synthesize g-C_3N_4, Fe_3O_4, and g-C_3N_4/Fe_3O_4 composites in various ratios. XRD confirmed the formation of g-C_3N_4, Fe_3O_4, and a g-C_3N_4/Fe_3O_4 heterostructure. SEM confirmed the rod-shaped structure of Fe_2O_3 and the layered-like fabrication of g-C_3N_4. The E_g of g-C_3N_4/Fe_3O_4 was approximately 1.9 eV, making it a beneficial composite material for visible response in photocatalysis activity, which was confirmed by UV-Vis spectroscopy. Dielectrics were used to study ferrite nanoparticles and provide information on the mechanism of conductivity in the parts of the dielectric that responded to an applied alternating electric field. In polycrystalline ceramics, the resistive and capacitive grains, contributions, electrode specimen interfaces, and grain boundaries may all be distinguished using impedance analysis, a crucial tool for the study of complicated electrical performance. The g-C_3N_4/Fe_3O_4 composite material showed high photocatalytic activity against methylene blue (MB) dye.

KEYWORDS

nanoparticles, carbon nitride, iron oxide, photodegradation, methylene blue dye

1 Introduction

Water pollution has greatly increased due to industrialization, urbanization, and the absolute discharge of industrial and organic pollutants into water sources (Goel, 2006; Hussain et al., 2021). The large amounts of wastewater from many types of dyeing enterprises contain unused dyes and other chemicals (Shindhal et al., 2021). These pigments are mostly toxic and non-biodegradable (Najar and Najar, 2019). Pigment waste pollutes both subsurface and surface water, with negative consequences on vegetation and animals

(Chowdhary et al., 2020). Methylene blue (MB) is the most widely used thiazine stain in the fabric industry. Its harmful effects include gastrointestinal irritation, cyanosis, and skin irritation (Khan et al., 2022). Many chemical and physical techniques, including flocculation-coagulation, ion exchange, surface adsorption, degradation of photocatalytic systems, and chemical precipitation, have been used to solve the challenge of the elimination of the dye from contaminated water (Vishnu et al., 2022). Among these, photodegradation is better than alternative techniques. In the context of the fundamental investigational technique and the existence of semiconductors under adequate light exposure, organic dye particles decompose into straightforward non-toxic byproducts (Som et al., 2020). TiO_2, CuO, ZnO, and other materials have been extensively utilized as photocatalysts for semiconductor-assisted photocatalytic processes (Nemiwal et al., 2021). However, owing to their significant band gaps, which account for only approximately 3%–5% of sunlight, they only function as photocatalysts when exposed to ultraviolet (UV) light (Arora et al., 2022). Therefore, highly efficient visible-light catalysts remain the subject of extensive research due to their potential for numerous applications, including energy consumption and environmental pollution control.

The band gap of 2.7 electron volts (eV) of graphite-like carbon nitride (two-dimensional) (g-C_3N_4), which can absorb visible light, is a typical semiconductor; moreover, it is polymeric and a non-metal material (Hu et al., 2020). Owing to its proper band gap, high stability, and simple preparation method, g-C_3N_4 is mostly used in applications related to pollution degradation (Liu et al., 2021). Furthermore, researchers have worked hard to improve the effectiveness of g-C_3N_4 photocatalysis by doping it with non-metallic or metallic elements (Chi, 2021) or coupling it with other organic dyes (Gurylev, 2021), halides (Zhang et al., 2020), or semiconductors.

However, in nature, g-C_3N_4 nanomaterials are highly dissolved. They cannot be recycled or reused due to a lack of catalyst-friendly environments. Fe_3O_4 nanoparticles with an outer magnetic field in a solution can be easily removed as they exhibit super-para-magnetism. Fe_3O_4 synthesis is easy and has good magnetic properties compared to all other super-paramagnetic materials. The conduction and valence band edges of Fe_3O_4 were −0.24 eV and 1.44 eV, and −1.61 eV and 1.73 eV for g-C_3 N_4 (Hussain et al., 2023a; Hussain et al., 2023b). Therefore, it was suitable for making a heterostructure and suppressing the recombination rate. Both Fe_3O_4 and g-C_3N_4 have band gap energies in the visible region. Therefore, they cover a broad spectrum of light, resulting in increased photocatalytic activity (Hussain et al., 2022a; Hussain et al., 2022b). Consequently, Fe_3O_4-based nanoparticles have been used in different research fields, including drug distribution procedures (Li et al., 2011), solid-phase extraction [26], and lithium storage in lithium-ion batteries (Yang et al., 2014). Magnetic nanocomposites of Fe_3O_4 and TiO_2 are regularly used for pollutant degradation (Xuan et al., 2009; Jing et al., 2013). Therefore, combining Fe_3O_4 with g-C_3N_4 may increase nanomaterial durability and make it easier to extract Fe_3O_4/g-C_3N_4 nanocomposites from suspensions in external magnetic fields. By encouraging the charge carrier's separation, the heterostructure of g-C_3N_4 and Fe_3O_4 increases visible light absorption and suppresses the electron and hole recombination rates. Numerous amino groups have been identified on the edges and surfaces of g-C_3N_4 and form coordination compounds with metal ions. Therefore, the edges or surfaces of g-C_3N_4 can be doped with coordination doping caused by metal ions (Lai et al., 2023). Different photocatalysts have been used for contaminant removal, such as the methylene blue dye with g-C_3N_4 and Fe_3O_4. Comparative studies on the degradation of MO using g-C_3N_4 and Fe_3O_4 are listed in Table 1.

However, this study used a photocatalysis process to degrade the pollutants, utilizing optimized photocatalyst composites to achieve higher photocatalytic activity. We applied a facile approach for the synthesis of g-C_3N_4/Fe_3O_4 composites with different ratios, such as 1:1, 60:40, 70:30, 80:20, and 90:10. While different studies have reported the composites of g-C_3N_4/Fe_3O_4, ours is the first study to determine the optimized ratio for enhanced photocatalytic activity. We have largely increased the quantity of one material and decreased the quantity of the second material. In the 1:1 ratio, both materials show good structural, optical, and photocatalytic properties. These are magnetic and electrical materials; therefore, at a 1:1 ratio, these materials can be used in other optical, magnetic, and electronic instruments to increase efficiency and reduce device costs.

2 Experiments

Materials: Urea, iron chloride, iron sulfate $FeSO_4.7H_2O$ (99–100%), $FeCl_3.6H_2O$ (99.0%), ammonia (25–28%), and distilled water. All other solvents were purchased from Sigma-Aldrich and were 99.6% pure. The materials were used without further modification.

2.1 Fabrication of g-C_3N_4

g-C_3N_4 was synthesized at 550°C for 5 h during thermal polymerization (pyrolysis) using urea as a precursor, at a temperature of 5°C/min. After cooling, powdered g-C_3N_4 was obtained by grinding.

2.2 Fabrication of Fe_3O_4 and g-C_3N_4/Fe_3O_4 composite

By default, g-C_3N_4 (0.68 g) was dispersed in 90.0 mL of distilled water mixed with $FeCl_3$ (0.94 g) and $FeSO_4$ (1 g) before being added to 10 mL NH_4OH and stirring for 1 h at 70°C. Next, until the pH reached 10.0, the ammonia solution was added dropwise to the reaction mixture. The powder was obtained after centrifuging and washing three times with ethanol and distilled water. The particles were dehydrated at 70°C for 12 h. Composites of g-C_3N_4/Fe_3O_4 were prepared in ratios of 1:1, 50:50, 60:40, 70:30, 80:20, and 90:10 to study the effect on this change on the energy band gap (in eV) and its effect on MB dye degradation. Pellets were fabricated using the hydraulic press (Apex) from each composition's final product. By applying a pressure of 4 tons, each pellet's diameter was 10 mm. The pellets were then sintered in a muffle furnace for 2 h at 310°C. These pellets were used for the assessment of dielectric properties.

TABLE 1 Comparisons of MB degradation analysis reported in various studies.

Type of material	Removal efficiency (%)	Time (mins)	Reference
$g\text{-}C_3N_4/Fe_3O_4$	90	100	This study
$g\text{-}C_3N_4$	38.6	140	Mao et al. (2018)
$g\text{-}C_3N_4/ZnO$	90	360	Alharthi et al. (2020)
$g\text{-}C_3N_4/BiVO_4$	93	75	Zhang et al. (2021)
$FePc/Fe_3O_4$	78	120	Wang et al. (2009)
ZnO/Fe_3O_4	99.9	150	Dwivedi et al. (2021)
ZnO	84.7		
Fe_3O_4	37.1		

2.3 Characterizations

The crystal structure and phase development of the samples were assessed using a Rigaku D/MAX-IIA X-ray diffractometer (XRD). The wavelength was 1.5406 A° and ranged from 10 to 70°. A Nova-Nano scanning electron microscope (SEM) 450-FESEM was used to examine the morphological features of the produced specimens. The frequency-dependent dielectric characteristics of the present specimens were explored on a Wayne Kerr (6500 B) precision impedance analyzer with copper electrodes through 20 Hz to 20 MHz. The original synthesized material was in powder form. For dielectric measurements, pellets with diameters of 1.01 cm and thicknesses of 0.1 cm were made from powder using an Apex hydraulic press under a pressure of 4 tons for 2 min in each case. All processes were performed at room temperature.

2.4 Photocatalytic tests

The photocatalytic performances of the $Fe_3O_4/g\text{-}C_3N_4$ composites were tested in glass reactors. In an MB aqueous solution (60 mL, 5 mg L^{-1}), 0.020 g of the sample was dispersed in each experiment. The Xe lamp (500 W output) served as the light source. The chemical solution was agitated magnetically in the dark for 65 min to attain MB saturation absorption onto the catalyst before irradiation. The following equation was used to determine the percentage of MB degradation.

$$\eta = \frac{A_o - A_t}{A_o} \times 100\% \tag{1}$$

In Eq. 1, η, A_t, and A_0 represent the degradation efficiency, verified concentration at time "*t*", and initial concentration at "$t = 0$", respectively.

3 Results and discussion

3.1 X-ray diffraction

The XRD patterns of $g\text{-}C_3N_4$, Fe_3O_4, and their composites are shown in Figure 1A. The $g\text{-}C_3N_4$ nanosheets exhibited two stable peaks along with $g\text{-}C_3N_4$, indicating that the crystal structures of the nanosheets and bulk $g\text{-}C_3N_4$ were essentially the same. The reflection peak at 13.1° with an hkl value of (100), originating from lattice planes along the c-axis (Figure 1A), was less apparent in nano-sheets. The peak occurs due to the commonly decreasing layer planar size during the thermal oxidation etch of bulk $g\text{-}C_3N_4$. The $g\text{-}C_3N_4$ nanoparticles showed the same effect (Niu et al., 2012). Compared to bulk $g\text{-}C_3N_4$, the peak initiating from the repeated layering in nanosheets moved from 27.23° to an hkl value of (002), indicating closer spacing between the sheets. The individual layers in bulk $g\text{-}C_3N_4$ are said to be fluctuating but might be made planar by additional heating, leading to compact stacking. Since the gallery distance decreased due to annealing during thermal oxidation, a denser packing should have formed in our situation (Zhou and Qiu, 2019). In previous studies, the $g\text{-}C_3N_4$ pure XRD spectrum showed two prominent peaks at 2θ of 2.23 and 13.1° (Yang et al., 2020). Therefore, the normal distribution of the (002) interfacial diffraction peak high value may be the cause of the strong height of 27.23°, while the interlayer structure's (13.1°) significant value (100) may be the cause of the peak's strong height (Tang et al., 2018). The characteristic peaks (Figure 1A) of the $g\text{-}C_3N_4$ were prepared by urea, as shown by the aforementioned data and the crystal database JCPDS 87–1,526, which have no additional impurity peaks, showing that $g\text{-}C_3N_4$ was effectively synthesized. Because of the long-range interplanar layering of the aromatic structure, the sharp peak at 27.23° belongs to d = 0.324 nm and is identified as the (002) plane of bulk $g\text{-}C_3N_4$. The minor peak at 13.1° belongs to the (100) plane with d = 0.676 nm.

Figure 1A shows the formation of the Fe_3O_4 nanoparticles. The peak position hkl values of (220), (311), (400), (422), (511), and (440) are clearly visible, showing the presence of a crystalline spinel phase composed of magnetite (Fe_3O_4) iron oxide. In the composite 1:1 of $g\text{-}C_3N_4/Fe_3O_4$, the peak of $g\text{-}C_3N_4$ shows low intensity. This confirmed the formation of a heterostructure.

The $Fe_2O_3@g\text{-}C_3N_4$ (1:1) NCs' Raman spectra are depicted in Figure 1B. Fe_2O_3-NPs showed distinctive Raman bands with Raman shifts of 607, 410, 294, and 221 cm^{-1}, which corresponded to the E_{1g}, E_{1g}, E_{1g}, and A_{1g} Raman modes, respectively. Raman peaks were likewise examined at ~480, ~708, and ~760 for $g\text{-}C_3N_4$. The s-triazine ring was indicated by the strongest peak of $g\text{-}C_3N_4$ at 708 cm^{-1} (Kang et al., 2018). The production of an NC of $g\text{-}C_3N_4$ and

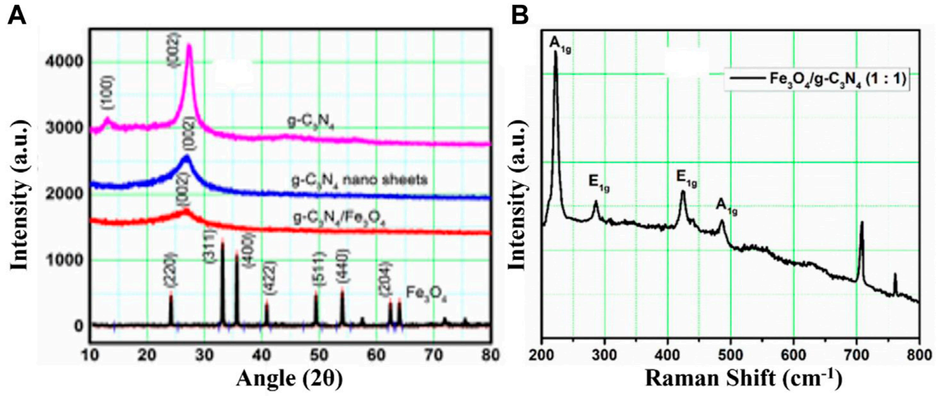

FIGURE 1
(A) XRD pattern and **(B)** Raman spectra of g-C_3N_4, g-C_3N_4 nano sheets, Fe_3O_4, and g-C_3N_4/Fe_3O_4 composites.

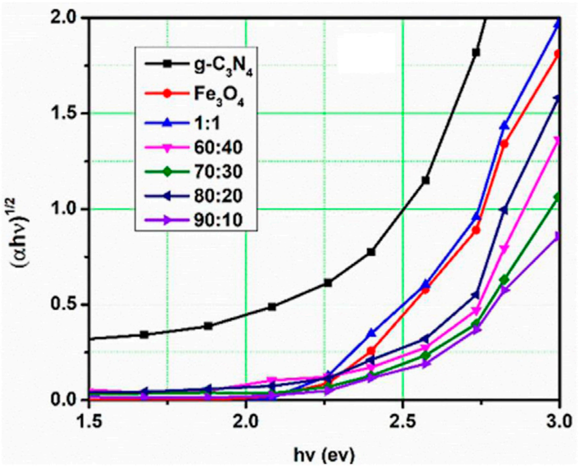

FIGURE 2
Tauc plot of g-C_3N_4, g-C_3N_4 nano sheets, Fe_3O_4, and g-C_3N_4/Fe_3O_4 composites.

Fe_3O_4 was confirmed by the presence of both g-C_3N_4 and Fe_3O_4 peaks.

3.2 UV-Vis spectroscopy and Raman analysis

The band gap energy (E_g) of the produced sample was derived by the following Tauc equation to fit the investigation's absorption data (Pareek et al., 2018; Zhu and Zhou, 2021).

$$(\alpha h\nu)^2 = A\left(h\nu - E_g\right), \qquad (2)$$

where hν and α are the photon energy and adsorption coefficient, respectively. The contact of the extended linear component of the (αhν) (Hussain et al., 2021) against the curve axis of the (hν) axis yields the E_g value. The E_g values of the g-C_3N_4/Fe_3O_4 nanocomposite, g-C_3N_4, and Fe_3O_4 are 1.9 eV, 2.7 eV, and 2.4 eV, respectively (Figure 2). These E_g values indicate that each compound and its nanocomposites were semiconductors in nature (Usman et al., 2019; Zhu and Zhou, 2021).

Figure 2 shows that the Eg of the composite g-C_3N_4/Fe_3O_4 prepared in the ratios of 1:1, 50:50, 60:40, 70:30, 80:20, and 90:10 decreased gradually to less than that of pure g-C_3N_4. Hence, the absorbance value of a pure g-C_3N_4 sample was lower than that for the composite g-C_3N_4/Fe_3O_4 ratios, which signified that composites were good photo-absorbers and photocatalysts.

3.3 Scanning electron microscopy (SEM) analysis

SEM micrographs of Fe_3O_4, g-C_3N_4, and their composites are shown in Figure 3. Fe_3O_4 showed a rod-like structure in SEM images. This structure is good for photocatalysis due to its high electron mobility. Regarding the weak van der Waals among layers in the graphite, g-C_3N_4 has a layered structure, while the assembly of the planar bonding is completely different.

The tri-s-triazine (heptazine) rings, which are connected to the structure's hypothesized aggregated mlem, are the energetically preferred form of g-C_3N_4. The composite materials showed both rod-like and layered structures, which confirmed the formation of composite materials.

Chemical mixing draws graphite with fewer or more pages while maintaining its composite structure. The main structure was composed of thick micron-sized particles evenly distributed throughout the sample area. Most of the particles had many full layers and hard surfaces.

3.4 Dielectric properties

Evaluation of the dielectric characteristics of ferrite nanoparticles provides information about the mechanism of conductivity in the parts of the dielectric that respond to an applied alternating electric field. These properties are dependent on various factors, such as the mode of production, chemical

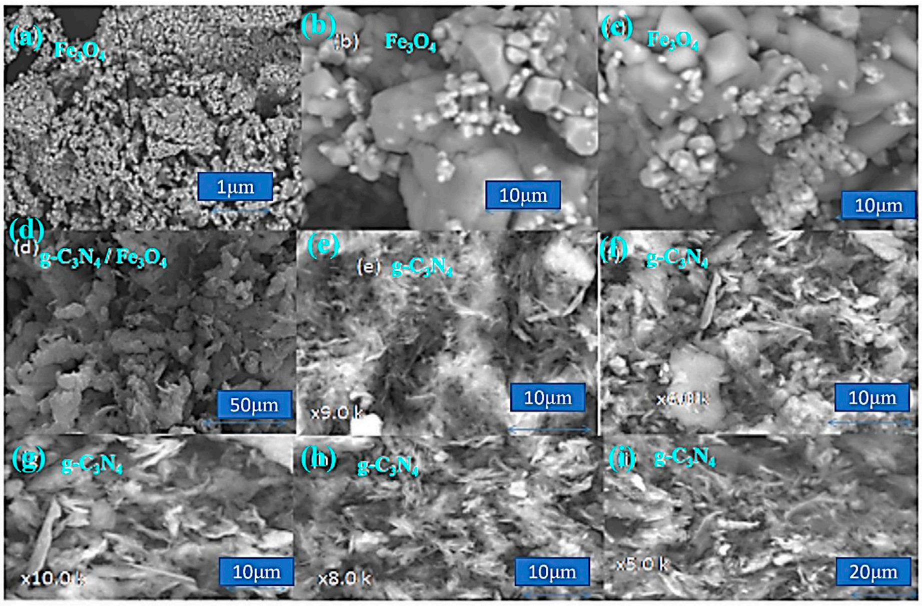

FIGURE 3
SEM micrographs of **(A–C)** Fe_3O_4, **(D)** g-C_3N_4/Fe_3O_4, and **(E–I)** g-C_3N_4.

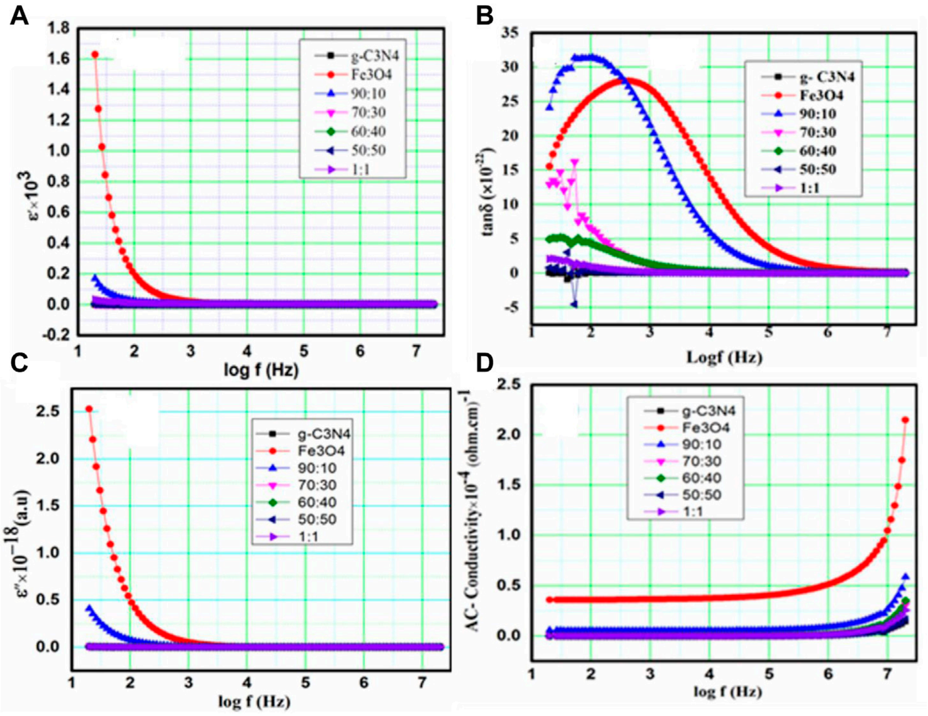

FIGURE 4
(A–D): Behaviors of the **(A)** dielectric constant (ε'), **(B)** dielectric loss angle (tanδ), **(C)** dielectric loss factor (ε''), and **(D)** AC conductivity (σ_{ac}) for the applied material frequencies.

composition, stoichiometry, porosity of the ion charge, particle size, and cation distribution between the octahedral and tetrahedral structures (Khan et al., 2020). In the current study, dielectric parameters, such as capacitance, and the dielectric loss angle (tan $\boldsymbol{\delta}$) were assessed using an LCR meter at room temperature. The real part of the permittivity (ε'), the imaginary part of the permittivity (ε'') or dielectric loss factor, and AC conductivity (σ_{ac}) are given by the following relationships (Hossen and Hossain, 2012; Zidi et al., 2015; Şaşmaz Kuru, 2020):

$$\varepsilon' = \frac{C_P\, d}{\varepsilon_{\circ} A}, \tag{3}$$

$$\varepsilon'' = \frac{\sigma_{ac}}{\omega \varepsilon_{\circ}}, \tag{4}$$

$$tan\, \delta = \frac{\varepsilon''}{\varepsilon'}, \tag{5}$$

$$\sigma_{ac} \frac{d}{Z' A}. \tag{6}$$

The capacitance of the pellet is represented by "C". Its unit is the farad. The thickness of the pellet is measured in meters, and its symbol is d. The cross-sectional area of the flat pellet surface is A. ε_o is the permeability of free space, and f is the frequency. Figures 4A–D show the behavior of ε', tan δ, and ε", respectively, at the applied frequency. The stored energy can be described by the permittivity (ε'). ε' has a higher value in the lower-frequency range and decreases with increasing frequency, consistent with the default behavior in most ferrite materials. The reduced ε' with greater frequency occurs because at higher frequencies, there is a time delay for each detected security. It also contributes to the polarization of the applied field (polarization cartridge damping), which leads to a reduced ε', and is assigned to the contribution to the electric polarizability (Prakash and Vasudevan, 2020). The reason for this change may be related to the $g\text{-}C_3N_4$ concentration, in which there is less of a chance to jump on grain boundaries. This will increase the grain boundary charge and, thus, the value of ε' changes (Patnaik et al., 2020). If the amount of iron ions is high, then the permittivity is high due to the presence of Fe ions in the S octahedral region (Khorsandi et al., 2021). Therefore, these ions can produce high polarization.

3.4.1 Variations in dielectric loss tangent (tanδ) and dielectric loss factor (ε′′) with frequency

Dielectric loss occurs due to energy dissipation in the dielectric materials and is explained in terms of tan δ and ε". It appears as a result of impurities and poor crystal lattice in the material, leading to polarization lagging of the supplied alternating field (Liu et al., 2020). Figures 4A, B show the variation in tan δ and ε", respectively, as a function of $log f$ at 27°C. The tan δ and ε" decrease with increasing frequency, which is the normal behavior of ferrites. The decreased ε" and tan δ values with the frequency were associated with the Maxwell–Wagner model and Koop's theory (Ünal et al., 2021). The sudden decline in dielectric constant, according to Kumar et al., is caused by inertia, which prevents immediate dipolar polarization. Polarizations with longer relaxation durations are frozen over a certain frequency (only electronic polarization mainly contributes); thus, the imaginary dielectric constant (ε") is decreased. The hopping of electrons between adjacent Fe ions (Fe^{3+} and Fe^{2+}) in the octahedral region requires only a tiny amount of energy in the high-frequency zone, which correlates with a small resistance (due to grains). Additionally, the grain boundaries are responsive and offer a high level of resistance in the low-frequency range. Consequently, significant energy is required to transfer electrons between two Fe ions. The energy lost in dielectrics is known as dielectric loss. Dielectric loss (tan δ) occurs because of crystal flaws such as secondary phases, defects, and delayed polarization with the applied field. As shown in Figure 4C, the tan δ values of Fe_3O_4, $g\text{-}C_3N_4$, and composite $g\text{-}C_3N_4/Fe_3O_4$ ratio systems demonstrated minimum and maximum values at high and low f, respectively. Koop's phenomenology theory explains why the dielectric energy loss and constant become frequency-independent at higher f. Substitution of $g\text{-}C_3N_4$ in the Fe_3O_4 sites increased both tan δ and ε". The trends shown by the samples in the current study design might be attributed to the combined influence of $g\text{-}C_3N_4/Fe_3O_4$ doping in composite ratios. The enhanced dielectric properties displayed by the specimens in later examination occurred due to the doping of $g\text{-}C_3N_4$ nanoparticles at Fe_3O_4 sites in the composite as the amount of $g\text{-}C_3N_4$ differed among the current compositions. Therefore, $g\text{-}C_3N_4$ can be used to improve the dielectric characteristics of the composites.

3.4.2 AC conductivity

The frequency-dependent AC conductivity (σ_{ac}) spectra of Fe_3O_4, $g\text{-}C_3N_4$, and composite $g\text{-}C_3N_4/Fe_3O_4$ are explained in Figure 4D. The spectra demonstrated that all samples have very low σ_{ac} values at low frequencies, indicating considerable resistance. After a certain high frequency, conductivity steadily increased. These types of processes are explained in Koop's model. This concept states that low conductivity at lower f is caused by weakly conducting grain boundaries, while strong conductivity at higher f is caused by highly conducting grains (Guo et al., 2021). The electron-hopping frequencies between Fe^{3+} and Fe^{2+} are severely hampered at lower frequencies (Wu and Zhu, 2019). Therefore, the observed conductivity of the material at a lower frequency is lower. However, as the frequency of the applied field rises, the conductive grain becomes highly active by promoting electron hopping between nearby ions and enhancing the interaction between ferrous iron (Fe^{2+}) and ferric iron (Fe^{3+}) ions on the octahedral sites. Consequently, the electrical conductivity increases with the frequency. The AC conductivity of $g\text{-}C_3N_4$ was low because the conductivity of polycrystalline materials declines with reducing grain size. Smaller grains contain more insulating grain borders and a smaller contact area between grains, which inhibit electron flow and, in turn, increase conductivity (Xi and Chung, 2021). In general, conductivity and permittivity are significantly influenced by grain size, stoichiometry, porosity, grain borders, and crystal defects.

3.4.3 Impedance analysis

In polycrystalline ceramics, impedance analysis is a crucial technique for separating resistive and capacitive grains, grain boundaries, and contributions, as well as electrode specimen interfaces, when studying complex electrical performances (Tiwari et al., 2020). The boundaries between grains are typically of a distinct conducting nature. This will depend on the nature of the sample used, and the temperature and frequency range of the test. The present study used dielectric materials with dipolar rotation in

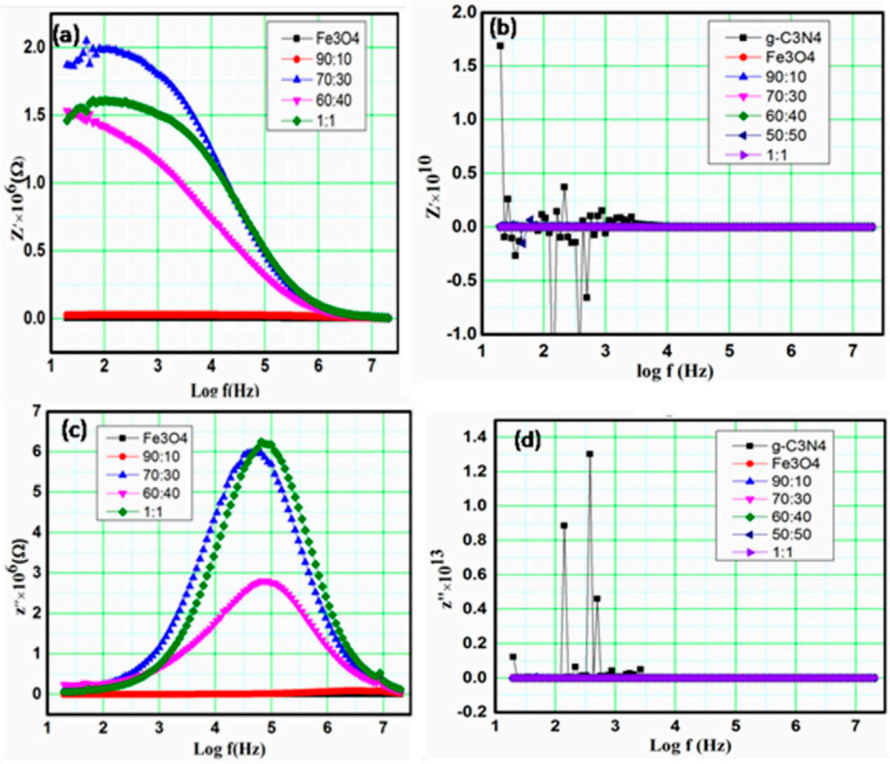

FIGURE 5
(A–D) Frequency dependence for real and imaginary parts of the electric impedance for Fe_3O_4, g-C_3N_4, and composite g-C_3N_4/Fe_3O_4 with different ratios.

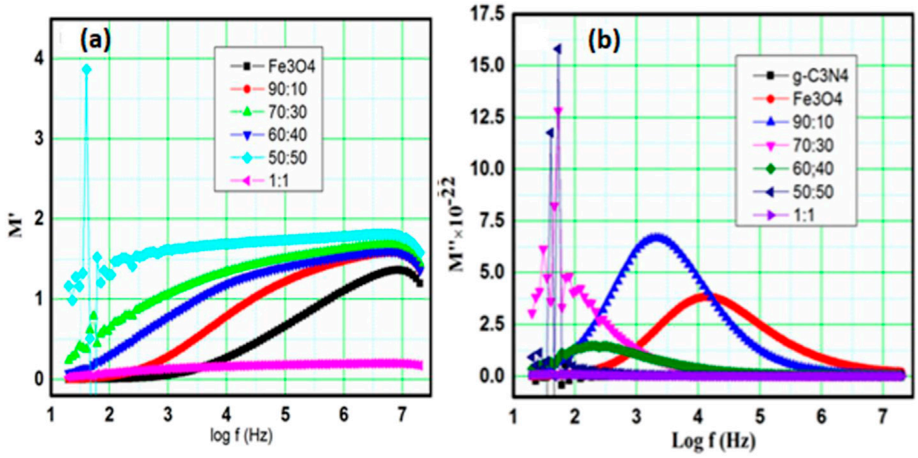

FIGURE 6
Frequency-dependent **(A)** real and **(B)** imaginary moduli of Fe_3O_4, g-C_3N_4, and composite g-C_3N_4/Fe_3O_4 with different ratios.

their electrical properties, as well as materials used in electronic conduction, for impedance spectroscopy studies.

Figures 5A–D show the impedance spectroscopy output characteristics as a sequence of semi-circles with various radii and/or origins. The electrical phenomena representation occurs because of the grain boundaries, grains, and interface polarization when their graph is drawn in the complex plane (Mazen et al., 2021). The electrical conductivity was measured using AC-impedance analysis, which showed that depending on their chemical composition, a wide range of materials with electric, anti-ferroelectric, or paraelectric phases and slightly different dielectric properties formed crystal structures of varying sizes. Understanding

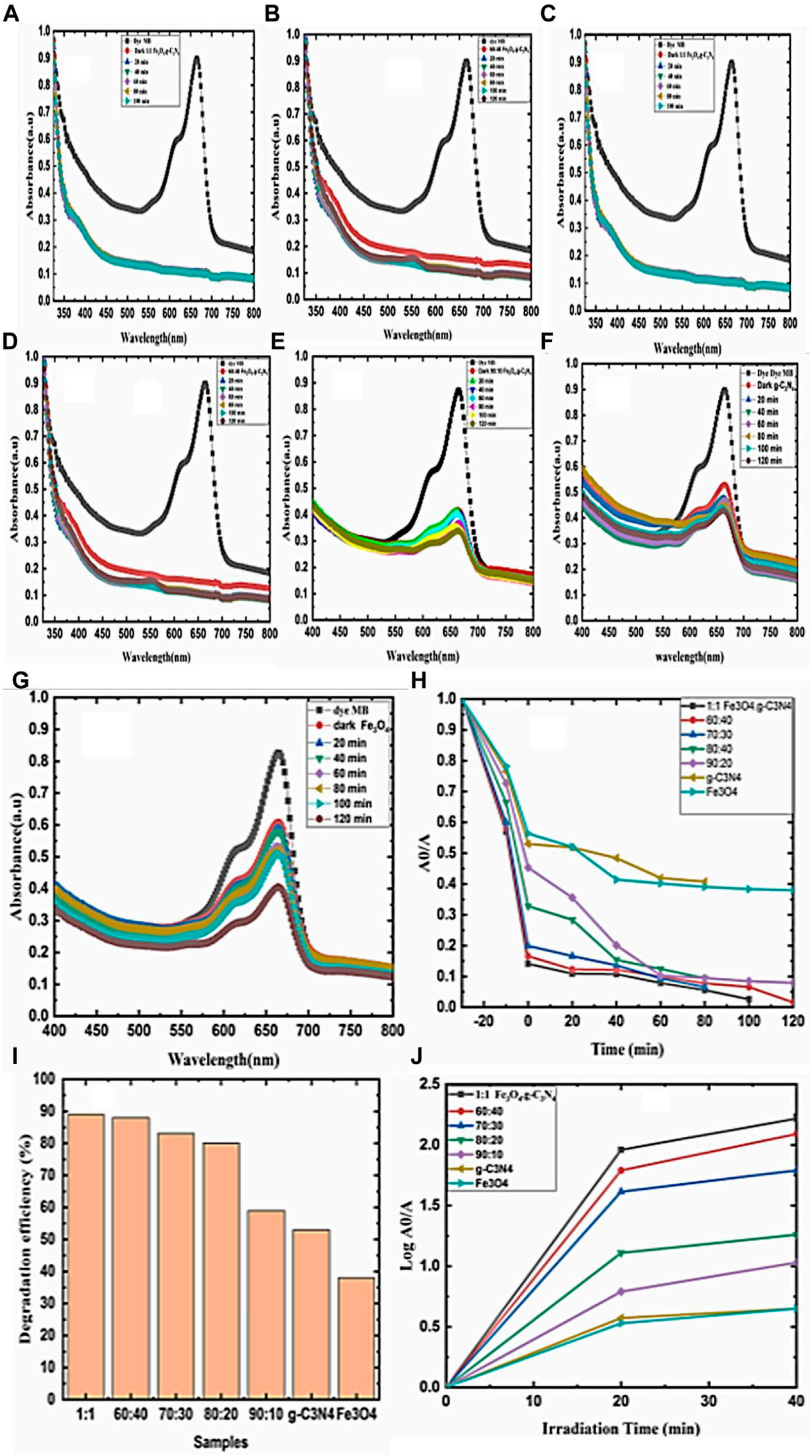

FIGURE 7
(A–G) Relationship between wavelength and absorbance. **(H)** Relationship between time and A_0/A. **(I)** Relationship between samples and degradation efficiency. **(J)** Relationship between log A_0/A and irradiation time.

the electrical conductivity of this type of ferroelectric and its physical characteristics is crucial (Fu et al., 2021). The internal defects in the material, such as the A-site vacancy, electron space charges, or oxygen, have significant effects on the electrical conductivity of the material. Therefore, it is important to have a basic understanding of their mechanics and the methods in the context of the defect mechanisms because of the different types of faults that are recommended for the relaxation of insulation material in high temperature ranges (Krauskopf et al., 2020). The formulas for impedance are as follows (Jha, 2013):

$$Z' = \frac{R}{1 + (\omega RC)\hat{}2}, \tag{7}$$

$$Z'' = \frac{\omega R\hat{}2C}{1 + (\omega RC)\hat{}2}. \tag{8}$$

3.4.4 Modulus study

The modulus spectroscopy of graphs helps us identify the spectral components of the material; those showing a different capacitance but the same resistance. The e-modulus formula also has the benefit of suppressing the electrode effect (Oliveira et al., 2019). Therefore, this is the optimal method for learning the spectroscopy of complex moduli. The value of the electric modulus (M*) can be estimated based on the following: The formulas for real modulus and imaginary modulus are as follows (Joshi et al., 2017; Rayssi et al., 2018):

$$M' = (\varepsilon')\big/(\varepsilon'\hat{}2 + \varepsilon''\hat{}2), \tag{9}$$

$$M'' = \frac{(\varepsilon'')}{(\varepsilon'^{\wedge 2} + \varepsilon''^{\wedge 2})}. \tag{10}$$

The complex electric module of formalization and analysis revealed the nature of polycrystalline and grain boundary effects. Figure 6 displays the complex modulus spectrum for M′ and M′, in which the arc was the electrical phenomenon with the lowest capacity to perform in a high-voltage system. Arcs appearing in the spectra demonstrate the ceramic's phase characteristics. In addition, the non-semi-circular arc proved that electrical relaxation phenomena existed in the Behera.

Figure 6A shows the relationship of M′ with frequency. Except for g-C_3N_4, for which the real modulus M′ stayed essentially the same over the whole frequency range, M′ increased to a maximum value with greater frequency for all samples. This clarified the large frequency range across which relaxation processes occur. For g-C_3N_4, Fe_3O_4 = 0, which verified that the real modulus M′ remained the same because of g-C_3N_4 and other composite samples as a result of Fe_3O_4 and g-C_3N_4. Owing to the charge carriers' limited mobility, conduction phenomena may be present. Figure 6B depicts the frequency-dependent imaginary component of the electrical modulus M′′. As the frequency and Fe_3O_4 content increased (up to 90%), the imaginary modulus M shifted to the high-frequency side. This is considered a non-Debye type of relaxation because the maximum peaks on either side of M″ are asymmetric and wider, demonstrating the distribution of relaxation periods rather than a single time constant (Arya and Sharma, 2018). The real modulus M″ maximum shifted toward a small frequency area for sample 70:30, indicating greater conduction. Therefore, at lower and higher frequencies, charge carriers can travel over short and long distances, respectively. The maximum real modulus M″ indicates a change in mobility from long to short range. The asymmetric modulus peaks will move in the direction of a higher frequency, which demonstrated the relationship between the movements of the mobile ion charges. The non-Debye type is implied by the asymmetry in the peak broadening due to a spread in the relaxation time caused by various time constants. The presence of low-frequency peaks points to the possibility of long-distance ion transport, while high-frequency peaks point to the possibility of ion confinement in a potential well.

3.5 Photocatalytic activity

The photocatalytic activity (PCA) values of the degradation of the methylene blue dye under visible light for g-C_3N_4, Fe_3O_4, and g-C_3N_4/Fe_3O_4 composites (1:1, 60:40, 70:30, 80:20, and 90:10) were 53, 38, 89, 88, 83, 80, and 59, respectively.

3.5.1 Evaluation of the photo-catalytic activity

The rate constant of the photo-degradation kinetics of the MB is shown in Figures 7A–J). Fe_3O_4 has a small PCA compared to MB under visible light irradiation, while Fe_3O_4/g-C_3N_4 nano-composites and g-C_3N_4 nanosheets were effective under the same conditions. In the nano-composite materials, the electrons migrated easily to Fe_3O_4 NPs due to the lower conduction band (CB) of Fe_3O_4 compared to g-C_3N_4. Thus, the PCA improved and the rate of photogenerated electrons and holes was effectively reduced. The 1:1 NC showed the highest PCA (89%). However, photogenerated electrons (e^-) have strong reductive properties. Photogenerated holes (h^+) possess high oxidizing characteristics and can interact with MB to produce CO_2 and H_2O. They form OH ions when they react with H_2O or O_2. Therefore, an improved PCA of the iron oxide and Fe_3O_4/g-C_3N_4 nano-composite was obtained. Compared to the g-C_3N_4 nanosheets, the 1:1 nano-composites showed higher-level photocatalytic effects, which were attributed to their greater dispersibility when combined with Fe_3O_4 nanocomposites. Owing to the reduced amounts of g-C_3N_4 in the 80:20, 70:30, and 60:40 nanocomposites compared to the g-C_3N_4 nanosheets, they showed weaker catalytic effects.

4 Conclusion

In conclusion, this study used solid-state reactions and sol-gel techniques to synthesize g-C_3N_4, Fe_3O_4, and g-C_3N_4/Fe_3O_4 with diverse proportions of g-C_3N_4 and Fe_3O_4. The formation of nano-sheet structures of g-C_3N_4, the cubic phase of Fe_3O_4, and g-C_3N_4/Fe_3O_4 nano-composites were confirmed by XRD. In SEM, Fe_3O_4 showed a rod-like structure, g-C_3N_4 showed a layered-like structure, and the composites showed both rod-like and layered-like structures. The composites at the 1:1 ratio showed a small E_g, according to UV-Vis spectroscopy. This is due to the formation of defective sites at the junction of two semiconductors. The PCA of the magnetically separated g-C_3N_4/Fe_3O_4 catalysts under visible light illumination was up to 1.8 times greater for MB dye compared with the pure g-C_3N_4. Owing to the synergistic interactions between Fe_3O_4 and g-C_3N_4, which increase the migratory performance of photo-generated charge carriers, the PCA is boosted. Our findings indicate the new design possibilities of the solutions reported here open the field for recycled photocatalysts that are magnetically separable and have good visible light PCA.

Data availability statement

The raw data supporting the conclusion of this article will be made available by the authors, without undue reservation.

Author contributions

AA: writing original draft; MA: revision and methodology; MT: writing original draft; SA: supervision and project administration; AH: manuscript revision; IA: contribution to the structural properties; AM: funding and project administration; MUF: supervision and project administration; MAF: explanation of optical analysis.

Acknowledgments

The authors would like to acknowledge the Researchers Supporting Project number (RSP2023R43), King Saud University, Riyadh, Saudi Arabia.

Conflict of interest

The authors declare that the research was conducted in the absence of any commercial or financial relationships that could be construed as a potential conflict of interest.

The handling editor FI declared a shared affiliation with author SA at the time of the review.

Publisher's note

References

Alharthi, F. A., Ali Alghamdi, A., Alanazi, H. S., Alsyahi, A. A., and Ahmad, N. (2020). Photocatalytic degradation of the light sensitive organic dyes: Methylene blue and rose bengal by using urea derived g-C3N4/ZnO nanocomposites. *Catalysts* 10 (12), 1457. doi:10.3390/catal10121457

Arora, I., Chawla, H., Chandra, A., Sagadevan, S., and Garg, S. (2022). Advances in the strategies for enhancing the photocatalytic activity of TiO2: Conversion from UV-light active to visible-light active photocatalyst. *Inorg. Chem. Commun.* 143, 109700. doi:10.1016/j.inoche.2022.109700

Arya, A., and Sharma, A. (2018). Structural, electrical properties and dielectric relaxations in Na+-ion-conducting solid polymer electrolyte. *J. Phys. Condens. Matter* 30 (16), 165402. doi:10.1088/1361-648x/aab466

Chi, Z. (2021). *Prospects for the application of advanced oxidation technology in the treatment of pharmaceutical wastewaters*.

Chowdhary, P., Bharagava, R. N., Mishra, S., and Khan, N. (2020). "Role of industries in water scarcity and its adverse effects on environment and human health," in *Environmental concerns and sustainable development* (Berlin, Germany: Springer), 235–256.

Dwivedi, P., Jatrana, I., Khan, A. U., Satiya, H., and Khan, M. (2021). Photoremediation of methylene blue by biosynthesized ZnO/Fe3O4 nanocomposites using callistemon viminalis leaves aqueous extract: A comparative study. *Nanotechnol. Rev.* 10 (1), 1912–1925. doi:10.1515/ntrev-2021-0117

Fu, D. W., Gao, J. X., Huang, P. Z., Ren, R., Shao, T., Han, L., et al. (2021). Observation of transition from ferroelasticity to ferroelectricity by solvent selective effect in anilinium bromide. *Angew. Chem. Int. Ed.* 60 (15), 8198–8202. doi:10.1002/anie.202015219

Goel, P. (2006). *Water pollution: Causes, effects and control*. New Delhi: . New age international.

Guo, F., Zhang, X., Cai, H., Fan, X., Hu, L., Sun, W., et al. (2021). Effect of doping location induced anisotropy on thermophysical properties of dilute Fe2O3-Y2O3-ZrO2 solid solutions. *J. Am. Ceram. Soc.* 104, 4742–4758. doi:10.1111/jace.17858

Gurylev, V. (2021). *Nanostructured photocatalyst via defect engineering: Basic knowledge and recent advances*. Berlin, Germany: Springer.

Hossen, M. B., and Hossain, A. A. (2012). *AC resistivity and frequency dependence of the dielectric properties for Al doped NiCuZn ferrites*. United States: IEEE, 903–907.

Hu, X., Hu, J., Peng, Q., Ma, X., Dong, S., and Wang, H. (2020). Construction of 2D all-solid-state Z-scheme g-C3N4/BiOI/RGO hybrid structure immobilized on Ni foam for CO2 reduction and pollutant degradation. *Mater. Res. Bull.* 122, 110682. doi:10.1016/j.materresbull.2019.110682

Hussain, A., Ali, N., Ali, S., Hou, J., Aslam, I., Naeem, H., et al. (2022). Diverse morphological study for nonmetal-doped g-C3N4 composites with narrow bandgap for improved photocatalytic activity. *Res. Chem. Intermed.* 48 (7), 2857–2870. doi:10.1007/s11164-022-04750-5

Hussain, A., Hou, J., Tahir, M., Ali, S., Rehman, Z. U., Bilal, M., et al. (2022). Recent advances in BiOX-based photocatalysts to enhanced efficiency for energy and environment applications. *Catal. Rev.* 22, 1–55. doi:10.1080/01614940.2022.2041836

Hussain, A., Hou, J., Tahir, M., Wang, X., Qadri, M. U., Jiang, T., et al. (2021). Fine-tuning internal electric field of BiOBr for suppressed charge recombination. *J. Environ. Chem. Eng.* 9 (1), 104766. doi:10.1016/j.jece.2020.104766

Hussain, A., Maqsood, S., Ji, R., Zhang, Q., Farooq, M. U., Boota, M., et al. (2023). Investigation of transition metal-doped graphitic carbon nitride for MO dye degradation. *Diam. Relat. Mater.* 132, 109648. doi:10.1016/j.diamond.2022.109648

Hussain, A., Tahir, M., Yang, W., Ji, R., Zheng, K., Umer, M., et al. (2023). Synergic effect among activated carbon/sulphur-assisted graphitic carbon nitride for enhanced photocatalytic activity. *Diam. Relat. Mater.* 135, 109836. doi:10.1016/j.diamond.2023.109836

Jha, A. (2013). Electrical characterization of zirconium substituted barium titanate using complex impedance spectroscopy. *Bull. Mater. Sci.* 36 (1), 135–141. doi:10.1007/s12034-013-0420-0

Jing, J., Li, J., Feng, J., Li, W., and William, W. Y. (2013). Photodegradation of quinoline in water over magnetically separable Fe3O4/TiO2 composite photocatalysts. *Chem. Eng. J.* 219, 355–360. doi:10.1016/j.cej.2012.12.058

Joshi, J., Kanchan, D., Joshi, M., Jethva, H., and Parikh, K. (2017). Dielectric relaxation, complex impedance and modulus spectroscopic studies of mix phase rod like cobalt sulfide nanoparticles. *Mater. Res. Bull.* 93, 63–73. doi:10.1016/j.materresbull.2017.04.013

Kang, S., Jang, J., Pawar, R. C., Ahn, S-H., and Lee, C. S. (2018). Low temperature fabrication of Fe_2O_3 nanorod film coated with ultra-thin g-C_3N_4 for a direct z-scheme exerting photocatalytic activities. *RSC Adv.* 8, 33600–33613. doi:10.1039/c8ra04499f

Khan, I., Bilal, A., Shakeel, K., and Malik, F. T. (2022). Effects of nickel toxicity on various organs of the Swiss albino mice. *Uttar Pradesh J. Zoology* 43 (14), 1–12.

Khan, M. Z., Gul, I. H., Baig, M. M., and Khan, A. N. (2020). Comprehensive study on structural, electrical, magnetic and photocatalytic degradation properties of Al3+ ions substituted nickel ferrites nanoparticles. *J. Alloys Compd.* 848, 155795. doi:10.1016/j.jallcom.2020.155795

Khorsandi, K., Hosseinzadeh, R., Sadat Esfahani, H., Keyvani-Ghamsari, S., and Ur Rahman, S. (2021). Nanomaterials as drug delivery systems with antibacterial properties: Current trends and future priorities. *Expert Rev. anti-infective Ther.* 19, 1299–1323. doi:10.1080/14787210.2021.1908125

Krauskopf, T., Richter, F. H., Zeier, W. G., and Janek, Jr (2020). Physicochemical concepts of the lithium metal anode in solid-state batteries. *Chem. Rev.* 120 (15), 7745–7794. doi:10.1021/acs.chemrev.0c00431

Lai, C., Ma, D., and Yi, H., 2023, Functional partition of Fe and Ti Co-doped G-C3n4 for photo-fenton degradation of OTC: Performance, mechanism, and dft study. *Sep. Purif. Technol.*, 306, 122546. doi:10.1016/j.seppur.2022.122546

Li, X., Huang, X., Liu, D., Wang, X., Song, S., Zhou, L., et al. (2011). Synthesis of 3D hierarchical Fe3O4/graphene composites with high lithium storage capacity and for controlled drug delivery. *J. Phys. Chem. C* 115 (44), 21567–21573. doi:10.1021/jp204502n

Liu, W., Ye, T., Jägermeyr, J., Müller, C., Liu, X., Shi, P., et al. (2021). Recent developments of doped g-C3N4 photocatalysts for the degradation of organic pollutants. *Crit. Rev. Environ. Sci. Technol.* 51 (8), 751–790. doi:10.1080/10643389.2020.1734433

Liu, Z., Yang, W., Wu, R., Hu, Q., Qiao, G., Liu, S., et al. (2020). A new quantitative analysis method for electromagnetic energy dissipation in microwave absorption materials. *J. Magnetism Magnetic Mater.* 516, 167332. doi:10.1016/j.jmmm.2020.167332

Mao, Y., Wu, M., Li, G., Dai, P., Yu, X., Bai, Z., et al. (2018). Photocatalytic degradation of methylene blue over boron-doped g-C3N4 together with nitrogen-vacancies under visible light irradiation. *React. Kinet. Mech. Catal.* 125 (2), 1179–1190. doi:10.1007/s11144-018-1414-0

Mazen, S., Nawara, A., and Abu-Elsaad, N. (2021). Investigation of dielectric behavior in Ni0. 7-xZn0. 3MxFe2O4 (M= Mn/Co/Cu) ferrites by impedance spectroscopy. *Ceram. Int.* 47 (7), 9856–9865. doi:10.1016/j.ceramint.2020.12.127

Najar, M. H., and Najar, I. A. (2019). An overview to photo-catalytic degradation of dyes in waste water. *Appl. Chem. Eng.* 2 (2). doi:10.24294/ace.v1i4.615

Nemiwal, M., Zhang, T. C., and Kumar, D. (2021). Recent progress in g-C3N4, TiO2 and ZnO based photocatalysts for dye degradation: Strategies to improve photocatalytic activity. *Sci. total Environ.* 767, 144896. doi:10.1016/j.scitotenv.2020.144896

Niu, P., Zhang, L., Liu, G., and Cheng, H. M. (2012). Graphene-like carbon nitride nanosheets for improved photocatalytic activities. *Adv. Funct. Mater.* 22 (22), 4763–4770. doi:10.1002/adfm.201200922

Oliveira, F., Dencheva, N., Lanceros-Méndez, S., Nunes, T., and Denchev, Z. (2019). Binary polyamide hybrid composites containing carbon allotropes and metal particles with radiofrequency shielding effect. *Polym. Compos.* 40 (S2), E1338–E1352. doi:10.1002/pc.24993

Pareek, S., Sharma, M., Lal, S., and Quamara, J. K. (2018). Polymeric graphitic carbon nitride–barium titanate nanocomposites with different content ratios: A comparative investigation on dielectric and optical properties. *J. Mater. Sci. Mater. Electron.* 29 (15), 13043–13051. doi:10.1007/s10854-018-9426-0

Patnaik, S., Sahoo, D. P., and Parida, K. (2020). Recent advances in anion doped g-C3N4 photocatalysts: A review. *Carbon* 172, 682–711. doi:10.1016/j.carbon.2020.10.073

Prakash, K., and Vasudevan, K. (2020). *Design and development of compact circularly polarized multiband and ultra-wideband microstrip antennas for wireless applications*. Kochi, Kerala: Cochin University of Science and Technology.

Rayssi, C., Kossi, S. E., Dhahri, J., and Khirouni, K. (2018). Frequency and temperature-dependence of dielectric permittivity and electric modulus studies of the solid solution Ca 0.85 Er 0.1 Ti 1− x Co 4x/3 O 3 (0≤ x≤ 0.1). *Rsc Adv.* 8 (31), 17139–17150. doi:10.1039/c8ra00794b

Şaşmaz Kuru, T. (2020). Room temperature structural, dielectric, and conductivity properties of AlxCd1-xFe2O4 ferrites. *J. Aust. Ceram. Soc.* 56 (2), 453–460. doi:10.1007/s41779-019-00349-z

Shindhal, T., Rakholiya, P., Varjani, S., Pandey, A., Ngo, H. H., Guo, W., et al. (2021). A critical review on advances in the practices and perspectives for the treatment of dye industry wastewater. *Bioengineered* 12 (1), 70–87. doi:10.1080/21655979.2020.1863034

Som, I., Roy, M., and Saha, R. (2020). Advances in nanomaterial-based water treatment approaches for photocatalytic degradation of water pollutants. *ChemCatChem* 12 (13), 3409–3433. doi:10.1002/cctc.201902081

Tang, Q., Meng, X., Wang, Z., Zhou, J., and Tang, H. (2018). One-step electrospinning synthesis of TiO2/g-C3N4 nanofibers with enhanced photocatalytic properties. *Appl. Surf. Sci.* 430, 253–262. doi:10.1016/j.apsusc.2017.07.288

Tiwari, B., Babu, T., and Choudhary, R. (2020). AC impedance and modulus spectroscopic studies of Pb (Zr0. 35-xCexTi0. 65) O3 (x= 0.00, 0.05, 0.10, 0.15) ferroelectric ceramics. *Mater. Chem. Phys.* 256, 123655. doi:10.1016/j.matchemphys.2020.123655

Ünal, B., Almessiere, M., Slimani, Y., Korkmaz, A. D., and Baykal, A. (2021). A study on the electrical and dielectric properties of SrGdxFe12− xO19 (x= 0.00–0.05) nanosized M-type hexagonal ferrites. *J. Mater. Sci. Mater. Electron.* 32, 18317–18329. doi:10.1007/s10854-021-06373-9

Usman, F., Dennis, J. O., Seong, K. C., Yousif Ahmed, A., Meriaudeau, F., Ayodele, O. B., et al. (2019). Synthesis and characterisation of a ternary composite of polyaniline, reduced graphene-oxide and chitosan with reduced optical band gap and stable aqueous dispersibility. *Results Phys.* 15, 102690. doi:10.1016/j.rinp.2019.102690

Vishnu, D., Dhandapani, B., Authilingam, S., and Sivakumar, S. V. (2022). A comprehensive review of effective adsorbents used for the removal of dyes from wastewater. *Curr. Anal. Chem.* 18 (3), 255–268. doi:10.2174/1573411016999200831111155

Wang, K., Yu, L., Yin, S., Li, H., and Li, H. (2009). Photocatalytic degradation of methylene blue on magnetically separable FePc/Fe3O4 nanocomposite under visible irradiation. *Pure Appl. Chem.* 81 (12), 2327–2335. doi:10.1351/pac-con-08-11-23

Wu, H., and Zhu, X. (2019). Microstructures, magnetic, and dielectric properties of Ba-doped BiFeO3 nanoparticles synthesized via molten salt route. *J. Am. Ceram. Soc.* 102 (8), 4698–4709. doi:10.1111/jace.16348

Xi, X., and Chung, D. (2021). Dielectric behavior of graphite, with assimilation of the AC permittivity, DC polarization and DC electret. *Carbon* 181, 246–259. doi:10.1016/j.carbon.2021.05.020

Xuan, S., Jiang, W., Gong, X., Hu, Y., and Chen, Z. (2009). Magnetically separable Fe3O4/TiO2 hollow spheres: Fabrication and photocatalytic activity. *J. Phys. Chem. C* 113 (2), 553–558. doi:10.1021/jp8073859

Yang, J., Li, J., Qiao, J., Lian, H., and Chen, H. (2014). Solid phase extraction of magnetic carbon doped Fe3O4 nanoparticles. *J. Chromatogr. A* 1325, 8–15. doi:10.1016/j.chroma.2013.11.052

Yang, X., Tian, Z., Chen, Y., Huang, H., and Hu, J. (2020). One-pot calcination preparation of graphene/g–C3N4–Co photocatalysts with enhanced visible light photocatalytic activity. *Int. J. hydrogen energy* 45 (23), 12889–12902. doi:10.1016/j.ijhydene.2020.03.028

Zhang, T-S., Hao, W-J., Wang, R., Wang, S-C., Tu, S-J., and Jiang, B. (2020). Electrocatalytic three-component annulation-halosulfonylation of 1, 6-enynes toward 1-indanones using sodium halides as both halogen sources and electrolytes. *Green Chem.* 22 (13), 4259–4269. doi:10.1039/d0gc00771d

Zhang, X., Li, M., Liu, C., Zhang, Z., Zhang, F., and Liu, Q. (2021). Enhanced the efficiency of photocatalytic degradation of methylene blue by construction of Z-scheme g-C3N4/BiVO4 heterojunction. *Coatings* 11 (9), 1027. doi:10.3390/coatings11091027

Zhou, D., and Qiu, C. (2019). Study on the effect of Co doping concentration on optical properties of g-C3N4. *Chem. Phys. Lett.* 728, 70–73. doi:10.1016/j.cplett.2019.04.060

Zhu, D., and Zhou, Q. (2021). Nitrogen doped g-C3N4 with the extremely narrow band gap for excellent photocatalytic activities under visible light. *Appl. Catal. B Environ.* 281, 119474. doi:10.1016/j.apcatb.2020.119474

Zidi, N., Chaouchi, A., D’Astorg, S., Rguiti, M., and Courtois, C. (2015). Impedance spectroscopy studies on (Na0. 5Bi0. 5) 0.94 Ba0. 06TiO3+ 0.3 wt% Sm2O3+ 0.25 wt% LiF lead-free piezoelectric ceramics. *Bull. Mater. Sci.* 38 (3), 731–737. doi:10.1007/s12034-015-0888-x